Nanoscale Advances

ROYAL SOCIETY OF CHEMISTRY

PAPER

View Article Online
View Journal | View Issue

Cite this: *Nanoscale Adv.*, 2025, **7**, 1892

Deep co-deposition of polydopamine in PVDF hydrogel to enhance photothermal evaporation efficiency†

Yu Ma, *[ab] Lan Yang,[a] Shangdi Wu,[a] Liran Xu[a] and Hua Huang*[a]

Polydopamine (PDA) is a widely utilized photothermal conversion material recognized for its ease of synthesis and environmental friendliness. However, its relatively weak light absorption capabilities lead to lower photothermal efficiency, restricting its application in solar steam generation (STG) processes. To effectively enhance light absorption, this study introduces a deep co-deposition method for the microstructural design of STG membranes. Unlike traditional surface co-deposition methods, which coat a layer of PDA on the membrane surface, the deep co-deposition method allows for the incorporation of PDA within the internal nanohydrogel structural units of the membrane. This approach significantly increases the PDA loading, resulting in a marked enhancement of light absorption capabilities. In the near-infrared region (800–2500 nm), where the light absorption of PDA is relatively weak, the absorbance improved from 70.18% (surface co-deposition) to 88.20% (deep co-deposition). While PDA has been extensively studied across various fields, its application as a structural and functional additive in hydrogels remains limited, particularly in comparison to the rapid advancements in PDA-based surface-engineered hydrogels. Thus, this study may provide valuable insights for related research areas.

Received 20th November 2024
Accepted 5th February 2025

DOI: 10.1039/d4na00963k

rsc.li/nanoscale-advances

Introduction

In the last ten years, there has been a notable increase in the interest surrounding solar-driven evaporation as a practical and eco-friendly method for generating fresh water from sources such as brine and sewage.[1–6] The technology known as solar-steam generation (STG) utilizes porous structures that absorb light to convert solar energy directly into heat, promoting efficient water evaporation.[7] This approach to seawater desalination stands out because it does not rely on fossil fuels, presenting a promising option for tackling severe water scarcity challenges through sustainable, low-carbon methods.[8]

Since 2013, polydopamine (PDA) has emerged as a prominent photothermal conversion material,[9] primarily due to its similarities to natural melanin, particularly regarding its photothermal efficiency in tumour therapies.[10] This efficiency originates from its 5,6-dihydroxyindole (DHI) and 5,6-indolequinone (IQ) structures, which form electron donor–acceptor pairs that reduce the band gap of PDA, thereby giving its photothermal properties.[11] However, due to its relatively lower evaporation efficiency, PDA is often not directly applied to the STG process.[12,13] The polymerization of dopamine involves a series of uncontrolled reactions and supramolecular aggregations, resulting in a low concentration of light-absorbing structures within PDA,[11] which significantly diminishes its evaporation efficiency compared to carbon-based materials or polypyrrole.[13] Furthermore, the complexity of this reaction mechanism complicates the regulation of the photothermal efficiency of PDA.[14] Consequently, due to the strong adhesive universality and good hydrophilicity of PDA, as well as its certain photothermal efficiency, most research currently utilizes PDA primarily as a hydrophilic modifier in STG membranes or as a binding agent for highly absorptive materials,[15,16] with its direct application in solar-steam generation being relatively rare. Thus, harnessing PDA to innovate new types of STG membranes could better leverage its advantages in hydrophilicity, antioxidant properties, antibacterial activity, and environmental friendliness in the STG process.[17]

At this point, researchers have identified four strategies to enhance the evaporation efficiency of polydopamine (PDA).[18,19] The first is the size strategy, which suggests that smaller PDA particles have superior optical absorption capabilities due to their varying geometric packing configurations. The second, known as the morphological strategy, indicates that PDA nanofibers outperform PDA nanoparticles (NPs) in terms of photothermal efficiency, which can be attributed to their increased conjugation. The third, termed the synergistic strategy, involves combining PDA with other reagents to form

[a]*China Coal Technology & Engineering Group Nanjing Design & Research Institute Co., Ltd, Nanjing, 210031, China. E-mail: mayutech03@gmail.com*

[b]*Guangdong Key Laboratory of Integrated Agro-environmental Pollution Control and Management, Guangdong Institute of Eco-environmental Science & Technology, Guangzhou, 510650, China*

† Electronic supplementary information (ESI) available. See DOI: https://doi.org/10.1039/d4na00963k

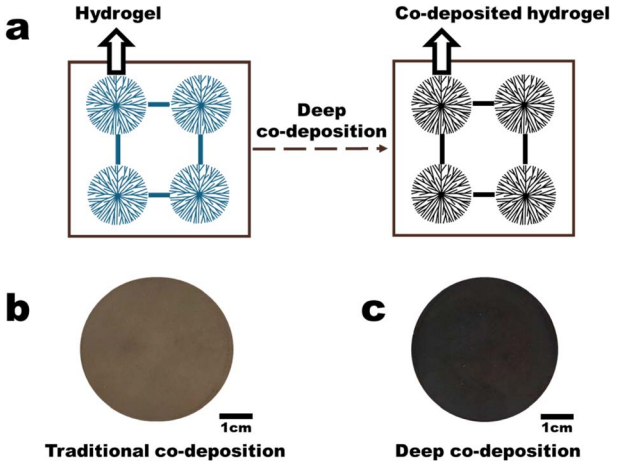

Fig. 1 (a) Schematic illustration of the deep co-deposition method; (b) digital image of a traditional co-deposited PVDF membrane under one solar illumination of 1 kW m^{-2} (wet state); (c) digital image of a deep co-deposited PVDF membrane under a solar illumination of 1 kW m^{-2} (wet state).

donor–acceptor structures that improve electron delocalization and decrease the energy gap. The fourth strategy, referred to as the pile-up strategy, demonstrates that after multiple cycles of co-deposition, the PDA content on the base membrane increases, thereby enhancing the light-absorbing structures within the PDA and ultimately resulting in a highly efficient solar-steam generation membrane.[19] Of these strategies, the pile-up strategy specifically utilizes a well-established co-deposition method to create an effective STG membrane. This fabrication process is straightforward, simple, and reproducible. Hence, the current study intends to explore new design concepts to optimize and refine the pile-up strategy.

This study employs the co-deposition method to load PDA-based materials into a PVDF hydrogel membrane, resulting in an internal gel co-deposited membrane, referred to as the deep co-deposition method (Fig. 1). Unlike traditional surface co-deposition methods, deep co-deposition significantly enhances the PDA content and the concentration of light-absorbing structures, thereby substantially improving evaporation efficiency in a single step. Moreover, PDA and PVDF used in this study are justifiably due to their unique advantages, with widespread of PVDF use in efficient, stable water treatment membranes aligning with future engineering trends[20] and conformal modification of PDA *via* mussel-inspired chemistry offering non-toxic, biodegradable photothermal properties.[3,21]

Results and discussion

Fabrication procedure of the PDA-gel membrane

The fabrication process of the deep co-deposited PDA gel (PDA-gel) membrane requires the co-deposition of PDA based on the fabrication of the PVDF hydrogel (PVDF-H) membrane (Fig. 2a). In our previous study,[22] the fabrication procedure and mechanism of the PVDF-H membrane have been thoroughly described. In brief, PVDF nanoparticle (PVDF NP) dispersion

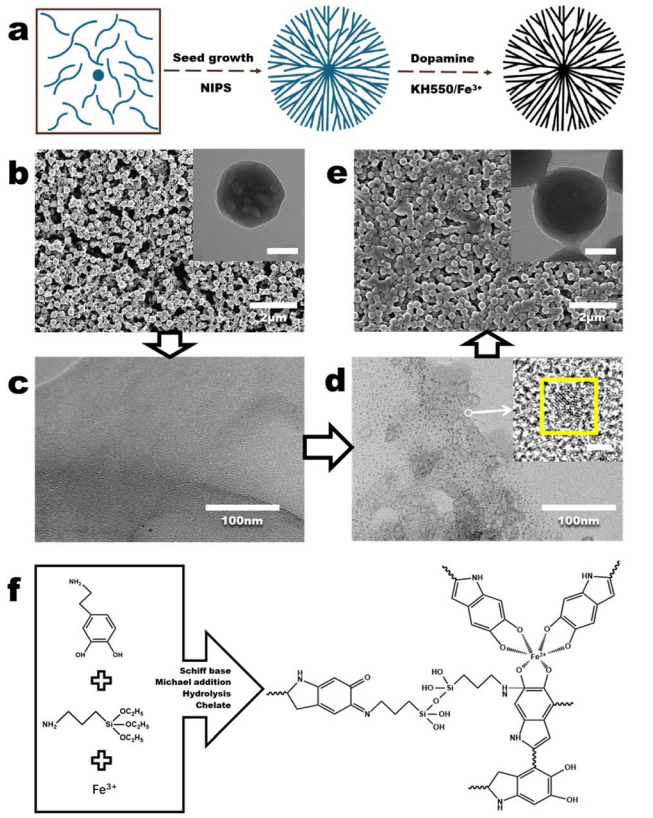

Fig. 2 Fabrication procedure of the PDA-gel membrane. (a) Schematic illustration of the formation of the PVDF hydrogel and the deep co-deposition of the PVDF hydrogel; (b) FESEM image of the PVDF NP aggregates, with the inset showing the STEM image of a PVDF NP (scale bar: 100 nm); (c) STEM image of the casting solution; (d) STEM image of the casting solution after microphase separation, with the inset showing the STEM image of a crystal seed (scale bar: 2 nm); (e) FESEM image of the surface morphology of a PVDF-H membrane, with the inset showing the STEM image of a PVDF nanohydrogel; (f) illustration of the reaction mechanism of the co-deposition procedure.

was filtered to obtain PVDF NP aggregates (Fig. 2b). Next, dimethylformamide (DMF) was used to partially dissolve the PVDF NP aggregates. During the dissolution, the majority of the PVDF crystals undergo transformation into free polymers, while the remaining crystalline structures become evenly dispersed in the casting solution (Fig. 2c). Further filtration of the casting solution, microphase separation leads to the generation of crystal seeds (Fig. 2d). By applying the non-solvent induced phase separation (NIPS) process, areas with a high PVDF concentration (rich phase) restrict the mobility of free polymers, allowing the crystal seeds to grow and form nanohydrogels with uniform size and shape (a process known as self-seeding, Fig. 2e). Meanwhile, the high viscosity of the PVDF polymer causes it to draw and form threads in areas with a low PVDF concentration (poor phase), resulting in fiber-like polymers that connect between the nanohydrogels. Ultimately, a PVDF-H membrane is formed (inset in Fig. 2e).

Next, the deep co-deposition method was employed to load PDA into the nanohydrogel within the PVDF-H membrane to fabricate PDA-gel membrane. During the loading phase, KH550

is incorporated as an additive to strengthen the adhesion between dopamine and the nanohydrogel.[23] Meanwhile, Fe^{3+} ions function as regulators that enhance light absorption in polydopamine (PDA).[17,24] Fig. 2f depicts the interactions occurring among dopamine, KH550, and Fe^{3+} ions. With regard to dopamine, the oxidation process facilitates the covalent bonding of catecholamine groups, resulting in the formation of quinones. These quinone entities then undergo cyclization within the amine-terminated chains, leading to the generation of indole. This transformation is followed by additional oxidation and reorganization reactions, yielding a range of monomeric compounds and short-chain or oligomeric products, including indole derivatives that possess photothermal characteristics. As a result, some of these coupled products may further participate in coupling reactions (polymerization), while others can react with amine groups through Schiff base and Michael addition processes.[25] In relation to KH550, the amino group present in KH550 serves as a connector between the dopamine derivatives and the nanohydrogel, thereby improving the bonding strength among dopamine, KH550, and the nanohydrogel.[26] Moreover, PDA reacts with ferric ions, reducing them to ferrous ions. The oxidizing property of KH550 allows the Fe ions in the reaction system to remain in the ferric state, enabling them to chelate with more polydopamine (Fig. S1†). Concerning the Fe^{3+} ions, these ions coordinate with three catechol groups to form tris-Fe^{3+}-catechol complexes. Within this complex, the Fe^{3+} ions exhibit strong electron-withdrawing properties, acting as electron acceptors and interacting with catechol groups to generate multiple donor–acceptor pairs within the Fe-PDA system. In this nanoparticle system, dopamine acts as the ligand while Fe^{3+} is in a high oxidation state, making ligand-to-metal charge transfer (LMCT) the primary mode of electron transition. This transition involves the movement of charge from the phenolic oxygens to the vacant orbitals of Fe^{3+}. The LMCT that occurs between the electron acceptor (Fe^{3+}) and the electron donor (the intrinsic structural unit of PDA) plays a crucial role in regulating light absorption in polydopamine (Video S1†).[27]

Characteristics of the membranes obtained through the fabrication procedure

As shown in Fig. 3a, the PVDF-H3 membrane in the wet state is composed of interconnected nanoparticles, resulting in a relatively loose microstructure with distinct pore channels visible (the membrane was first freeze-dried and then characterized by FESEM). The PVDF-H3 membrane in the dry state was obtained by drying the wet PVDF-H3 membrane in an oven at 60 °C for 30 minutes. Fig. 3b indicates that the microstructure of the membrane in the dry state is dense, with no pore channels observed. The digital image in Fig. 3c reflects that the membrane has a larger area and is transparent in the wet state, while its area significantly reduces and transitions from a transparent state to an opaque white state in the dry state. These observations suggest that during the drying process, the volume of the microstructural units (nanoparticles) within the membrane may have undergone significant shrinkage, or the

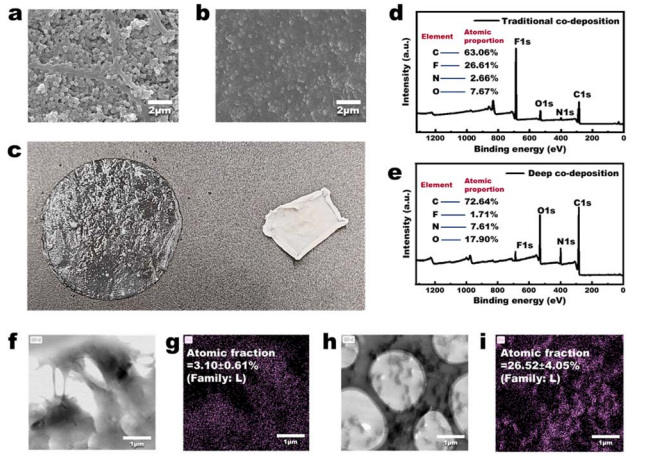

Fig. 3 Characteristics of the membranes obtained through the fabrication procedure. (a) FESEM image of the surface morphology of the PVDF-H3 membrane in the wet state; (b) FESEM image of the surface morphology of the PVDF-H3 membrane in the dry state; (c) digital image of the PVDF-H3 membrane in wet (left) and dry (right) state; (d) broad-scan XPS spectrum and atomic proportion of the control (PVDF-C) membrane; (e) broad-scan XPS spectrum and atomic proportion of the PDA-gel3 membrane; (f and h) STEM images of the PVDF-C membrane (f) and the PDA-gel3 membrane (h); (g and i) EDS maps showing the distribution of the Fe element in the PVDF-C membrane (g) and the PDA-gel3 membrane (i).

distance between these microstructural units has markedly decreased, leading to a transition of the membrane microstructure from loose to dense. Additionally, the reason for the membrane being transparent and having a larger area in the wet state is likely due to the presence of a certain amount of water within the membrane, which causes it to be in a swollen state. Moreover, the average DMT modulus of a PVDF-H membrane surface in the wet state is about 3.09 GPa (Fig. S2a†), while the average DMT modulus of the surface of commercial PVDF microfiltration membranes is about 7.58 GPa (Fig. S2b†). Therefore, the contact deformation of the PVDF-H3 membrane in the wet state is significantly greater than that of the commercial PVDF membrane (the DMT modulus describes the elastic behaviour of materials under contact deformation conditions), indicating that the PVDF-H3 membrane material is markedly 'soft' in the wet state, reflecting that it is a loosely cross-linked polymer structure. Thus, based on the definition of a gel—'polymers that interconnect under certain conditions to form a spatial network structure, with voids filled with a liquid serving as the dispersion medium'—and considering the consistency of the characterization results in Fig. 3 and S2† with this definition, along with the fact that the PVDF-H membrane is composed of interconnected nanoparticles, it can be confirmed that the PVDF-H membrane in the wet state is composed of nanohydrogels.

As shown in Fig. 3d and e, after obtaining the PDA-gel membrane using the deep co-deposition method, the proportion of fluorine (F) elements in the membrane is significantly lower than that in the traditional PVDF co-deposition membrane (PVDF-C). Since there is no difference in the co-deposition method used in the fabrication processes of both

the PDA-gel and PVDF-C membranes, and only PVDF contains fluorine in the materials used for fabrication, the significantly reduced proportion of fluorine in the PDA-gel membrane indicates a substantial increase in the content of PDA within the PDA-gel membrane. Moreover, as mentioned above, Fe^{3+} serves as a regulator that enhances the light absorption capacity of PDA. Consequently, a higher concentration of Fe^{3+} (electron acceptor) within the membrane induces PDA (electron donor) to generate more light-absorbing structures. As shown in Fig. 3f–i, the distribution of iron (Fe) in the PVDF-C membrane is relatively uniform, with an atomic fraction of 3.10 ± 0.61% (Fig. 3f and g); in contrast, the distribution of iron (Fe) in the PDA-gel membrane is uneven, primarily concentrated within the nanohydrogel (as indicated by the grey area in Fig. 3h), with an atomic fraction of 26.52 ± 4.05% (Fig. 3i). This indicates that the content of Fe in the PDA-gel membrane is approximately 8.55 times higher than that in the PVDF-C membrane, resulting in a significant enhancement of light absorption capacity of the membrane. The macroscopic manifestation of this enhanced light absorption capability is illustrated in Fig. 1b and c: under one sun illumination (1 kW m^{-2}), the colour of the PVDF-C membrane appears brown, whereas the colour of the PDA-gel membrane appears black.

Morphologies of the membranes

Fig. 4a demonstrates that the commercial PVDF membrane has a porous structure. After the co-deposition of PDA, the PVDF-C membrane was obtained. Fig. 4b shows that the surface morphology of the PVDF-C membrane is not significantly different from that of the commercial PVDF membrane, and the internal morphology of the PVDF-C membrane is consistent with that of the surface (Fig. 4c). Moreover, Fig. 4g indicates the morphology of the PDA-gel3 membrane, which shows no significant difference compared to the PVDF-H3 membrane depicted in Fig. 3a, suggesting that the deep co-deposition process has a minimal impact on the geometric structure of the membrane. Fig. 4d–o show that as the volume of the DMF solution of PVDF added to water gradually increases (from 1 mL to 8 mL) during the preparation of the PVDF NPs, the resulting PDA-gel*X* membranes (where '*X*' represents the volume of the DMF solution) exhibit a transition in surface and internal morphology from a loose porous structure to a dense structure with fewer pores, and the thickness of the PDA-gel*X* membranes gradually increases as '*X*' increases. This indicates that the key control parameter for the structure of the PDA-gel membranes is the volume of the DMF solution; as this volume increases, the membrane structure becomes denser with fewer pore channels, and the thickness of the membrane also increases. Moreover, as illustrated in Fig. S3,† the pore size distribution of the PDA-gel*X* membranes remains largely consistent. Notably, with the exception of the PDA-gel1 membrane, which exhibits a relatively larger average pore size of 325.8 nm, the average pore sizes of the other PDA-gel membranes remain relatively unchanged, hovering around 200 nm. Remarkably, a significant alteration is observed in the porosity of the PDA-gel*X* membranes (Fig. S3b†). As '*X*' increases, the porosity decreases substantially, ranging from 80.95% for PDA-gel1 down to 28.09% for PDA-gel8. These findings suggest that the denser membrane structure observed in Fig. 4e, h, k and n is primarily attributed to the reduction in porosity, rather than a decrease in average pore size.

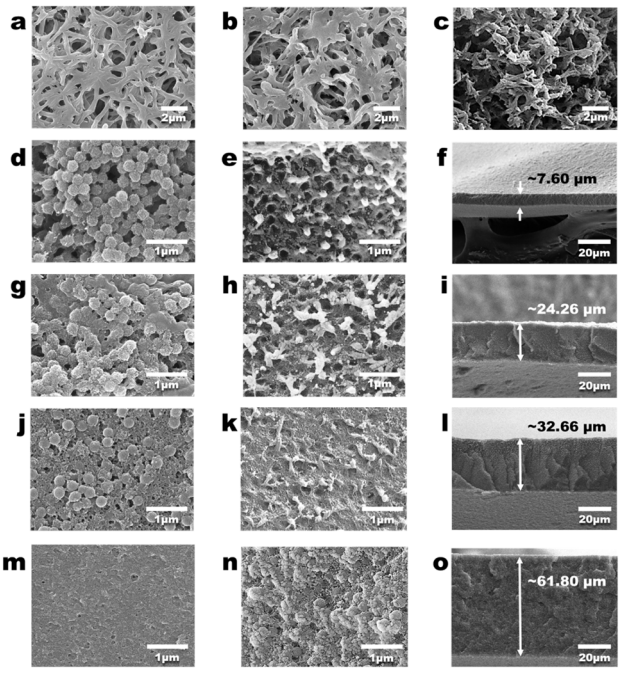

Fig. 4 Morphologies of the membranes. (a, b, d, g, j and m) FESEM images of the surface morphology of the commercial PVDF membrane (a), PVDF-C (b), PDA-gel1 (d), PDA-gel3 (g), PDA-gel5 (j), and PDA-gel8 (m) membranes; (c, e, f, g, i, k, l, n and o) FESEM images of the cross-sectional morphology of the PVDF-C (c), PDA-gel1 (e and f), PDA-gel3 (h and i), PDA-gel5 (k amd l), and PDA-gel8 (n and o) membranes.

Photothermal properties of the membranes

To experimentally evaluate the absorption capacity, we conducted measurements of the diffuse reflectance for various membranes, including PVDF, PVDF-C in the dry state, PDA-gel3 in the dry state, PVDF-C in the wet state, and PDA-gel3 in the wet state. As illustrated in Fig. 5a, the deep co-deposited membrane (PDA-gel3 in the wet state) exhibited exceptional absorption characteristics across the entire solar spectrum, with an average reflectance of less than 15% (specifically, 12.11%). This represents a substantial improvement compared to the traditional surface co-deposited membranes, which had a reflectance of 23.57% for PVDF-C in the wet state and 69.02% for PVDF-C in the dry state. Furthermore, as shown in Fig. 5b and Table 1, our findings indicate that PDA-gel3 in the wet state possesses the capability to absorb approximately 96.18% of UV radiation, 96.30% of visible light, and 88.20% of infrared solar irradiation. This results in a total absorption capacity of 93.13% across the entire solar spectrum, significantly surpassing the performance of PVDF-C in the wet state, which recorded absorption rates of 94.00% in the UV-vis range and 70.18% in the NIR range.

The significantly enhanced light absorption capability of the PDA-gel3 membrane compared to PVDF-C is primarily

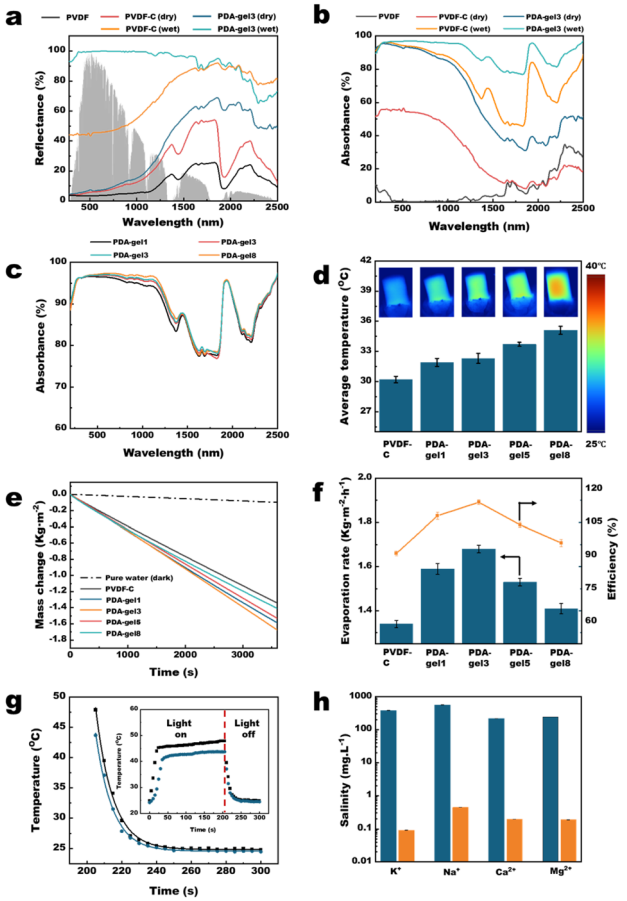

Fig. 5 Photothermal properties of the membranes. (a) Diffuse reflectance spectra of PVDF, PVDF-C in dry state, PDA-gel3 in dry state, PVDF-C in wet state and PDA-gel3 in wet state membranes. The inserted background is a solar irradiation spectrum (direct + circumsolar); (b) light absorption of the commercial PVDF membrane, PVDF-C membranes in wet/dry state, and PDA-gel3 membranes in wet dry state; (c) light absorption of the PDA-gel*X* membrane in wet state; (d) average surface temperature of the PVDF-C membrane and PDA-gel*X* membrane in wet state; (e) loss of pure water in a dark environment and loss of pure water under a illumination of 1 kW m^{-2} using PVDF-C and PDA-gel*X* membranes; (f) evaporation rates and efficiencies of PVDF-C and PDA-gel*X* membranes under a illumination of 1 kW m^{-2}; (g) the temperature relationship with time during light on and light off; (h) salt concentrations before and after desalination (simulated brine).

attributed to the deep co-deposition of PDA within the PVDF hydrogel. This process allows for a greater incorporation of PDA and an increase in light-absorbing structures, ultimately improving the absorption performance of the membrane (Fig. 3).

When focusing on the PVDF-C and PDA-gel3 membranes in their wet state, it was observed that the absorption rate of the PDA-gel3 membrane in the near-infrared (NIR, 800–2500 nm) range increased from 70.17% to 88.20% compared to the PVDF-C membrane (Fig. 5b). More interestingly, the corresponding absorption rates in the dry state for the PVDF-C and PDA-gel3 membranes were only 22.63% and 53.48%, respectively (Fig. 5b). The reason for this significant improvement is currently believed to be that the wet state does not adversely affect the light absorption properties of the PDA co-deposited membrane, as indicated by relevant studies.[19,29] The underlying mechanism is essentially similar to the observation in nature where sand or soil appears darker when wet. This darkening effect primarily stems from the shift in the particle-surrounding medium from air to water, resulting in a decrease in their relative refractive index. Subsequently, this reduction leads to an elevation in the average forward scattering degree, as evidenced by the asymmetry parameter (*i.e.*, the mean cosine of the scattering angle). It is widely recognized that natural media, such as sand and soil, which exhibit multiple scattering, become noticeably darker upon wetting. Consequently, photons incident on these media undergo a greater number of scattering events before they can emerge, thus enhancing their probability of being absorbed.[30]

Moreover, as shown in Fig. 5c, the light absorption of the PDA-gel*X* series increases with '*X*', with PDA-gel8 exhibiting the best absorption characteristics (96.41% in the UV-vis region and 88.89% in the NIR region). This trend indicates that a higher '*X*' correlates with an increased quantity of nanohydrogels in the PDA-gel*X* formulation, resulting in greater PDA loading and a higher density of light-absorbing structures. However, Fig. 5c also indicates that as '*X*' increases exponentially, there is no significant enhancement in the light absorption. This phenomenon indicates that the changes in the membrane surface structure have a relatively minor impact on its light absorption capability, indicating that specific light-trapping structures did not formed on the membrane surface.[31] Fig. 5d shows that the average temperature of the membrane surface gradually increases with the rise in '*X*'. However, Fig. 5e reveals that while the water evaporation rates of all PDA-gel membranes surpass that of PVDF-C, an examination of the PDA-gel membranes shows that the water evaporation rate of PDA-gel*X* initially increases and then decreases as '*X*' increases, with PDA-

Table 1 Solar absorption of photothermal materials in different spectrum region

Sample	Total (%)	UV[a] (%)	Visible[b] (%)	Infrared[c] (%)	Ref.
Solar	100.00	6.83	53.99	39.19	28
PVDF	4.38	0.37	0.20	3.81	This work
PVDF-C (dry)	41.93	3.75	29.31	8.87	This work
PDA-gel3 (dry)	77.31	6.47	49.89	20.96	This work
PVDF-C (wet)	84.46	6.49	50.47	27.50	This work
PDA-gel3 (wet)	93.13	6.57	51.99	34.57	This work

[a] UV light: <400 nm. [b] Visible light: 400–800 nm. [c] Infrared light: >800 nm.

gel3 performing the highest evaporation rate at 1.68 kg m^{-2} h^{-1}. This phenomenon can be elucidated by Fig. S4.† As shown in Fig. S4,† the water contact angles (WCAs) of PVDF-gel3 and PVDF-gel8 are 14.5 ± 0.2° and 11.9 ± 0.1°, respectively. However, the WCA of PDA-gel3 drops to 0° after 1.04 seconds, while PDA-gel8 takes 3.57 seconds to reach the same value.

In addition to these observations, the mechanism of intramembrane water transport is discussed in detail in the ESI materials.† The relationship between the intramembrane water transport rate and membrane structure in this study can be approximately calculated by combining the Hagen–Poiseuille equation[32] with the Young–Laplace equation:

$$J_v \approx \frac{\in \pi \delta r_p}{4\mu L} \quad (1)$$

where J_v is the flux (intramembrane water transport rate); r_p is the average pore radius of membrane; $\in$ is the porosity; and μ is the water viscosity; L is the membrane thickness; δ is the surface tension of water. As a result, by combining the porosity data from Fig. S3b† with the membrane thickness data from Fig. 4f, i, l and o, the flux of the PDA-gel*X* membranes can be approximately calculated as: 1.48×10^{-5} m s^{-1} for PDA-gel3 and 8.57×10^{-7} m s^{-1} for PDA-gel8. That is to say, the flux of the PDA-gel8 membrane is an order of magnitude lower than that of the PDA-gel3 membrane. These observations and the calculated results suggest that as '*X*' increases, the membrane structure becomes denser with fewer pore channels, and the thickness of the membrane also increases (Fig. 4d–o). This results in excessive mass transfer resistance within PDA-gel8, weakening fluid permeability and preventing timely replenishment of water lost due to evaporation, thereby reducing the evaporation rate.

Furthermore, by correlating Fig. 5c and d, it can be seen that while the light absorption rates of the PDA-gel membranes do not exhibit significant variation, the surface temperature of PDA-gel8 is markedly higher than that of PDA-gel3. This difference may be attributed to the lack of liquid water on the membrane surface, leading to a decrease in evaporation enthalpy and consequently resulting in a higher membrane surface temperature.[33]

The apparent evaporation efficiency was calculated using the formula:

$$\eta = \dot{m} h_{LV} / P \quad (2)$$

where $\dot{m}$ denotes the rate of evaporation when exposed to irradiation, h_{LV} represents the specific evaporation enthalpy of water, and P stands for the light power. For this research, we calculated the light power density according to the area of irradiation, and the observed apparent efficiency was established to reflect both solar and environmental evaporation, allowing this efficiency to surpass 100%. Consequently, the PDA-gel3 membrane achieved an impressive apparent evaporation efficiency of 114.10% (as shown in Fig. 5f).

Moreover, photothermal conversion efficiency between the deep co-deposition membrane (PDA-gel3) and the traditional surface co-deposition membrane (PVDF-C) were investigated by using the method introduced by Wu *et al.*[34] Specifically, the external photothermal conversion efficiency η_{ext} is determined by the quotient of the produced heat Q to the energy of photon flux irradiation q:

$$\eta_{ext} = Q/q \quad (3)$$

Under irradiation from solar light, the temperature of the material rises from ambient temperature T_{sur} to a maximum temperature T_{max}, where the heat generated by the material, Q, balances the heat lost to the surroundings, q:

$$Q = Q_{sur} = h \times s \times (T_{max} - T_{sur}) \quad (4)$$

where h refers to the heat transfer coefficient, and s is the surface area of the material for heat dissipation. As shown in Fig. S5,† the $T_{max} - T_{sur}^{max}$ of the PVDF-C and PDA-gel3 membranes were about 15.6 °C and 20.8 °C, respectively. Additionally, by applying eqn (S8)† to fit the cooling data from the experiments, the $h \times s$ values for the PVDF-C and PDA-gel3 membranes were determined to be around 3.93 mW $°C^{-1}$ and 3.96 mW $°C^{-1}$, (see the ESI materials for details†). Therefore, the external photothermal conversion efficiencies, η_{ext}, for the PVDF-C and PDA-gel3 membranes were calculated to be approximately 73.47% and 87.93%, respectively. It is important to highlight that, as illustrated in Table 1 and Fig. 5a and b, 93.13% of the total solar energy was absorbed according to the reflectance measurements. This indicates that the quantum efficiencies, which represent the ratio of absorbed photons to generated heat,[6,35] were 78.89% and 94.41% for the PVDF-C and PDA-gel3 membranes, respectively. In other words, the photothermal conversion efficiency and quantum efficiency of the PDA-gel3 membrane exhibited significant improvement compared to the PVDF-C membrane.

Fig. 5h depicts the salt rejection performance of the PDA-gel3 membrane, indicating that the concentrations of the four main ions were reduced by approximately two to three orders of magnitude following the desalination process. Furthermore, the PDA-gel3 membrane demonstrated a stable mass change rate over five evaporation cycles (Fig. S6a†) and maintained consistent mass change rates under 1 sun illumination in both pure water and brine solutions, as well as in weakly acidic, weakly alkaline solutions, and at higher temperatures (Fig. S6b, c and S7†). These results indicate that the membrane is highly suitable for long-term practical applications in solar-driven steam generation (STG).

Experimental

Materials

Commercial nylon membranes (average pore size = 0.22 μm, sourced from Tianjin Jinteng Experimental Equipment Co., Ltd, China) and a commercial polyvinylidene fluoride (PVDF) membrane (average pore size = 0.45 μm, supplied by Cytiva, USA) were acquired from their respective manufacturers. PVDF (with an average molecular weight of 0.4 MDa), *N*,*N*-dimethylformamide (DMF), 95% ethanol, NaOH, and γ-aminopropyl triethoxysilane (KH550) were obtained from Shanghai Macklin

Biochemical Co., Ltd, China. Additionally, dopamine hydrochloride and anhydrous $FeCl_3$ were purchased from Shanghai Aladdin Biochemical Technology Co. Ltd, China. All chemical reagents were utilized as received, without any further purification.

Synthesis of the PVDF nanoparticles (PVDF NPs)

The preparation of PVDF nanoparticles (NPs) followed the methodology established in our prior research.[22] In summary, 0.6 g of PVDF was completely dissolved in 100 mL of DMF at a temperature of 60 °C for 12 hours, resulting in a uniform PVDF solution. Once the solution cooled to 25 °C, a specified volume was mixed with 200 mL of deionized water to produce a dispersion of PVDF nanoparticles. The volume of the PVDF solution added during this process was adjusted as indicated in Table 2.

Fabrication of the PVDF hydrogel (PVDF-H) membrane

The preparation of PVDF-H membranes was conducted following the methods outlined in our earlier studies.[22] Initially, a commercial nylon microfiltration membrane with an average pore size of 0.22 μm and a diameter of 50 mm was placed in a vacuum filtration apparatus. Next, 200 mL of the PVDF nanoparticle dispersion was introduced into the filtration cup, which was then subjected to vacuum filtration at a pressure of 0.95 bar. This step allowed for the accumulation of PVDF nanoparticle aggregates on the surface of the membrane. To partially dissolve these aggregates, 20 mL of DMF was carefully added to the filtration cup, and vacuum filtration was continued at the same pressure of 0.95 bar until a uniformly dispersed slurry of PVDF polymer was obtained on the microfiltration membrane. Following this, the vacuum filtration process was maintained at 0.95 bar for an additional 7 minutes. Subsequently, 200 mL of water was meticulously introduced into the filtration cup and filtered under the same vacuum pressure to create a PVDF-H membrane that included a substrate. The final membrane was then immersed in ethanol to separate it from the substrate, and the freestanding membrane was stored in deionized water for later use. The various PVDF-H membranes produced are listed in Table 2.

Fabrication of the deep co-deposited PDA gel (PDA-gel) membrane

A solution was prepared by sequentially adding 0.4 g of dopamine hydrochloride, 20 mL of ethanol containing γ-aminopropyl triethoxysilane (KH550), and 0.2 g of $FeCl_3$ to 200 mL of deionized water. Following this, an ethanol-prewetted PVDF-H membrane was submerged in the resulting mixture. The reaction was allowed to proceed at 50 °C in a thermostatic incubator, with stirring at 150 rpm for a duration of 12 hours. After the reaction was complete, the resulting product was thoroughly rinsed with deionized water at least three times to ensure cleanliness for future applications. The PDA-gel membranes were then preserved in water prior to use. The PVDF-gel membranes produced are detailed in Table 2.

Table 2 Preparation parameters and nomenclature of the membrane

		Preparation parameters
PVDF-gel membrane	PVDF-H membrane	The volume of DMF solution of PVDF added to water (mL)
PDA-gel1	PVDF-H1	1
PDA-gel3	PVDF-H3	3
PDA-gel5	PVDF-H5	5
PDA-gel8	PVDF-H8	8

Fabrication of the control membrane

In a sequential manner, 0.4 g of dopamine hydrochloride, 20 mL of ethanol containing KH550, and 0.2 g of $FeCl_3$ were combined with 200 mL of deionized water. Following this, an ethanol-prewetted commercial PVDF membrane (45 mm in diameter) was immersed into the prepared solution. The mixture was stirred at 150 rpm for a period of 12 hours at a temperature of 50 °C within a thermostatic incubator. Upon completion of the reaction, the resultant product was thoroughly rinsed with deionized water at least three times to ensure cleanliness for future applications. The membrane used as a control was designated as the PVDF-C membrane.

Synthesis of PDA

Dopamine hydrochloride (0.4 g) was dissolved in deionized water (200 mL). NaOH (0.6 mL, 1 mol L) was added, and the solution was shaken (110 rpm) at 50 °C for 12 h. After the reaction was complete, the dispersion was filtrated by commercial nylon membranes (average pore size = 0.22 μm). The obtained sediments were dried using a vacuum oven (40 °C, 0.05 bar) before being subjected to characterization.

Synthesis of PDA-KH550

Dopamine hydrochloride (0.4 g) was dissolved in deionized water (200 mL); γ-aminopropyl triethoxysilane (KH550, 0.2 g) was dissolved in 20 mL ethanol. The ethanol solution was poured into the aqueous solution, stirred uniformly, and then shaken (110 rpm) at 50 °C for 12 hours. After the reaction was complete, the dispersion was filtrated by commercial nylon membranes (average pore size = 0.22 μm). The obtained sediments were dried using a vacuum oven (40 °C, 0.05 bar) before being subjected to characterization.

Synthesis of PDA-Fe

Dopamine hydrochloride (0.4 g) was dissolved in deionized water (200 mL); anhydrous iron chloride ($FeCl_3$, 0.2 g) was dissolved in 20 mL ethanol. The ethanol solution was poured into the aqueous solution, stirred uniformly, and then shaken (110 rpm) at 50 °C for 12 hours. After the reaction was complete, the dispersion was filtrated by commercial nylon membranes (average pore size = 0.22 μm). The obtained sediments were dried using a vacuum oven (40 °C, 0.05 bar) before being subjected to characterization.

Synthesis of PDA-KH550-Fe

Dopamine hydrochloride (0.4 g) was dissolved in deionized water (200 mL); $FeCl_3$ (0.2 g) and KH550 (0.2 g) was dissolved in 20 mL ethanol. The ethanol solution was poured into the aqueous solution, stirred uniformly, and then shaken (110 rpm) at 50 °C for 12 hours. After the reaction was complete, the dispersion was filtrated by commercial nylon membranes (average pore size = 0.22 μm). The obtained sediments were dried using a vacuum oven (40 °C, 0.05 bar) before being subjected to characterization.

Sample characterization

Membrane fabrication and sample preparation for characterization were conducted using a freeze dryer (FD-8, SIM International Group Co. Ltd, USA). The optical reflectance and absorbance of the resulting membrane samples was assessed with an ultraviolet-visible-near-infrared spectrophotometer (Agilent Cary 5000), which included an integrating sphere (Internal DRA-2500, Agilent). Additionally, a Fourier transform infrared (FTIR) spectrometer (Nicolet 5700) equipped with a mid-infrared integrating sphere (Pike Technologies) was utilized. The structural characteristics of both the surface and cross-section of the membranes were analysed using a field-emission scanning electron microscope (FESEM) system (TESCAN MIRA4, Oxford). For cross-sectional analysis, membranes were first cooled with liquid nitrogen and subsequently coated with gold *via* sputtering. Scanning transmission electron microscopy (STEM) images and energy-dispersive X-ray spectroscopy (EDS) maps were acquired using an FEI Talos-F200X system (Thermal Scientific Talos™) operating at 200 keV. To assess the elemental compositions and functional groups of the materials, X-ray photoelectron spectroscopy (XPS, 250Xi, Thermo Fisher) was performed with a Kα X-ray source (1486.60 eV) and an aluminium target. The concentrations of ions present in the brine sample were quantitatively analysed using inductively coupled plasma-optical emission spectrometry (PerkinElmer 8300). Finally, a contact angle goniometer (Data-Physics, OCA 50) was employed to measure the dynamic contact angle of the membrane in air. The pore sizes and porosities of the membranes were measured using a high-performance automatic mercury injection instrument (Micromeritics Instrument Corporation, AutoPore LV 9510).

Solar desalination

To begin the experiment, position the PDA-gel membranes, each measuring 2 cm × 1 cm, on a damp nonwoven fabric placed atop a cover glass, angled at 45° relative to the horizontal surface of the liquid. To minimize additional liquid loss from evaporation due to temperature fluctuations, seal both the liquid surface and the area where the cover glass meets the liquid with polystyrene foam. A solar simulator (7ILX500P, SOFN Instruments Co., Ltd) was employed to direct a solar beam onto the surface of the sample while monitoring the mass loss. An infrared camera (Fluke TiS65) was utilized to measure the temperature, and changes in mass due to evaporation were recorded using an electronic balance (ME204/02, Meter-Toledo Instruments Co., Ltd) with a precision of 0.1 mg. For assessing the mass change rate of the PDA-gel membrane in brine, the membrane was exposed to 1 sun for 10 minutes to allow its performance to stabilize. In cyclic testing, the PDA-gel3 membrane was rinsed every hour to maintain its original evaporation rate, with each cycle lasting 5 minutes. For test the photothermal conversion efficiency, the membranes were initially freeze-dried and then cut into circles with a diameter of 3.5 cm. Subsequently, they were placed on a non-woven fabric to test the change in membrane surface temperature over time under one solar illumination (1 kW m^{-2}). For the long-term evaluation, to test the membrane under different pH values, temperatures, and ion strengths, the mass change rate of the PDA-gel3 membrane was recorded every 4 hours from 9:00 AM to 9:00 PM over a period of 3 days, with each measurement lasting 5 minutes. Before each test, the membrane surface was thoroughly rinsed. Additionally, during the long-term evaluation testing under different temperatures, the membrane was placed flat on a non-woven fabric that was wrapped around polystyrene foam in the water. To evaluate the long-term stability of the membrane under continuous illumination of 1 sun in water, the membrane underwent an initial 10 minutes exposure to stabilize its performance. Subsequently, the PDA-gel3 membrane was tested once daily between 9:00 AM and 9:30 PM over a period of 10 days. The composition of the simulated brine utilized in these tests is detailed in Table 3.

Table 3 Composition of the brine

Content	Brine (mg L^{-1})
Total dissolved solids	3830
NaCl	1470
KCl	770
$MgCl_2$	920
$CaCl_2$	790

Conclusions

In summary, this study presents a deep co-deposition method for incorporating PDA-based materials into a PVDF hydrogel membrane, resulting in an internally gel co-deposited structure. The high swelling capacity suggests that the membrane is composed of cross-linked nanohydrogels. Compared to the surface co-deposition method, the significantly higher content of PDA and Fe^{3+} (a light absorption regulator) within the membrane indicates an increase in the quantity of light-absorbing structures, thereby greatly enhancing the light absorption capabilities of the membrane. Additionally, the study identified the content of PVDF nanohydrogel as a key parameter influencing the membrane microstructure; excessive amounts can lead to a dense, low-porosity structure. This density increases mass transfer resistance during solar steam generation (STG) processes, reducing fluid permeability and hindering the timely replenishment of water lost through

evaporation, ultimately decreasing the evaporation rate. As a result, the deep co-deposited membrane achieves a maximum evaporation rate of 1.68 kg m^{-2} h^{-1} and an apparent evaporation efficiency of 114.10%. Finally, the study demonstrates that the membrane exhibits exceptional desalination capabilities while maintaining long-term stability.

Data availability

Data supporting this article have been included as part of the ESI.†

Author contributions

Yu Ma conceived the idea and designed the experiments. Yu Ma, Lan Yang performed the fabrication and characterization of the membranes. Yu Ma, Shangdi Wu, and Liran Xu carried out performance evaluation experiments of the membranes. Hua Huang supervised the project. Yu Ma wrote the manuscript.

Conflicts of interest

There are no conflicts to declare.

Acknowledgements

This study was supported by the China Postdoctoral Science Foundation (2021M700889), the GDAS Special Project of Science and Technology Development (2022GDASZH-2022010105), Self-initiated Science and Technology Project of China Coal Technology & Engineering Group Nanjing Design & Research Institute Co., Ltd (CCTEGNJRD-PD2024N01), New Product Development (PD) Project of China Coal Technology & Engineering Group Nanjing Design & Research Institute Co., Ltd (CCTEGNJRD-PD 2025N01).

Notes and references

1 P. Tao, G. Ni, C. Y. Song, W. Shang, J. B. Wu, J. Zhu, G. Chen and T. Deng, *Nat. Energy*, 2018, **3**, 1031–1041.
2 O. A. Kazi, W. Chen, J. G. Eatman, F. Gao, Y. N. Liu, Y. Q. Wang, Z. J. Xia and S. B. Darling, *Adv. Mater.*, 2023, **35**, 2300913.
3 Y. J. Zheng, R. A. C. Gonzalez, K. B. Hatzell and M. C. Hatzell, *Joule*, 2021, **5**, 1971–1986.
4 X. L. Pan, Y. K. Jin, Y. Zhou, X. Q. Wang, W. H. Lu, J. Q. He and G. W. Ho, *Adv. Energy Mater.*, 2023, **13**, 2204095.
5 L. L. Zhu, T. P. Ding, M. M. Gao, C. K. N. Peh and G. W. Ho, *Adv. Energy Mater.*, 2019, **9**, 1900250.
6 M. M. Gao, L. L. Zhu, C. K. Peh and G. W. Ho, *Energy Environ. Sci.*, 2019, **12**, 841–864.
7 W. Shang and T. Deng, *Nat. Energy*, 2016, **1**, 16133.
8 P. J. J. Alvarez, C. K. Chan, M. Elimelech, N. J. Halas and D. Villagán, *Nat. Nanotechnol.*, 2018, **13**, 634–641.
9 F. F. Liu, X. Liu, F. Chen and Q. Fu, *Prog. Polym. Sci.*, 2021, **123**, 101472.
10 L. H. Wang, K. Y. Song, C. Jiang, S. P. Liu, S. R. Huang, H. Yang, X. L. Li and F. Zhao, *Adv. Healthcare Mater.*, 2024, **13**(28), 2401451.
11 Y. Zou, X. F. Chen, P. Yang, G. J. Liang, Y. Yang, Z. P. Gu and Y. W. Li, *Sci. Adv.*, 2020, **6**, eabb4696.
12 L. F. Cui, P. F. Wang, H. N. Che, J. Chen, B. Liu and Y. H. Ao, *Chem. Eng. J.*, 2023, **477**, 147158.
13 H. C. Yang, F. Lu, H. N. Li, C. Zhang, S. B. Darling and Z. K. Xu, *Adv. Funct. Mater.*, 2023, **33**, 2304580.
14 P. Yang, S. Zhang, X. F. Chen, X. H. Liu, Z. Wang and Y. W. Li, *Mater. Horiz.*, 2020, **7**, 746–761.
15 C. J. Wei, X. H. Zhang, S. Y. Ma, C. X. Zhang, Y. Li, D. J. Chen, H. Jiang, Z. K. Xu and X. J. Huang, *Chem. Eng. J.*, 2021, **425**, 130118.
16 Y. R. Chen, R. K. Xin, X. C. Huang, K. C. Zuo, K. L. Tung and Q. L. Li, *J. Membr. Sci.*, 2021, **620**, 118913.
17 H. Li, Y. Jia, S. Bai, H. Peng and J. Li, *Adv. Colloid Interface Sci.*, 2024, **334**, 103316.
18 Y. T. Xu, J. F. Hu, J. J. Hu, Y. Y. Cheng, X. C. Chen, Z. P. Gu and Y. W. Li, *Prog. Polym. Sci.*, 2023, **146**, 101740.
19 S. L. Wu, L. N. Quan, Y. T. Huang, Y. T. Li, H. C. Yang and S. B. Darling, *ACS Appl. Mater. Interfaces*, 2021, **13**, 39513–39522.
20 V. O. C. Concha, L. Timoteo, L. A. N. Duarte, J. O. Bahu, F. L. Munoz, A. P. Silva, L. Lodi, P. Severino, J. Leon-Pulido and E. B. Souto, *J. Mater. Sci.*, 2024, **59**, 14185–14204.
21 H. Omidian and R. L. Wilson, *Materials*, 2024, **17**, 3916.
22 Y. Ma, X. L. Zhao and B. He, *Nanoscale Adv.*, 2024, **6**, 3543–3552.
23 S. Li, X. Li, M. C. Shao, J. L. Yang, Q. H. Wang, T. M. Wang and X. R. Zhang, *Tribol. Int.*, 2019, **140**, 105861.
24 Y. Jia, F. Gao, P. Z. Wang, S. W. Bai, H. Li and J. B. Li, *J. Colloid Interface Sci.*, 2024, **676**, 626–635.
25 Y. L. Liu, K. L. Ai and L. H. Lu, *Chem. Rev.*, 2014, **114**, 5057–5115.
26 L. Zhou, Y. He, H. Shi, G. Q. Xiao, S. H. Wang, Z. Y. Li and J. Y. Chen, *J. Hazard. Mater.*, 2019, **380**, 120865.
27 N. Xu, A. Hu, X. M. Pu, J. F. Li, X. M. Wang, J. Wang, Z. B. Huang, X. M. Liao and G. F. Yin, *ACS Appl. Mater. Interfaces*, 2022, **14**, 15894–15910.
28 C. A. Gueymard, *Sol. Energy*, 2004, **76**, 423–453.
29 H. C. Yang, R. Z. Waldman, M. B. Wu, J. W. Hou, L. Chen, S. B. Darling and Z. K. Xu, *Adv. Funct. Mater.*, 2018, **28**, 1705327.
30 S. A. Twomey, C. F. Bohren and J. L. Mergenthaler, *Appl. Opt.*, 1986, **25**, 431–437.
31 Y. Xia, Y. Kang, Z. Y. Wang, S. Yuan, Y. Li, L. Gao, H. T. Wang and X. W. Zhang, *J. Mater. Chem. A*, 2021, **9**, 6612–6633.
32 S. Déon, A. Escoda and P. Fievet, *Chem. Eng. Sci.*, 2011, **66**, 2823–2832.
33 X. Z. Hu, W. C. Xu, L. Zhou, Y. L. Tan, Y. Wang, S. N. Zhu and J. Zhu, *Adv. Mater.*, 2017, **29**, 1604031.
34 J. Wang, Y. Y. Li, L. Deng, N. N. Wei, Y. K. Weng, S. Dong, D. P. Qi, J. Qiu, X. D. Chen and T. Wu, *Adv. Mater.*, 2017, **29**, 1603730.
35 X. H. Liu, D. D. Mishra, X. B. Wang, H. Y. Peng and C. Q. Hu, *J. Mater. Chem. A*, 2020, **8**, 17907–17937.